



Article

Photodetection Properties of MoS₂, WS₂ and Mo_xW_{1-x}S₂ Heterostructure: A Comparative Study

Maryam Al Qaydi ^{1,2}, Ahmed Kotbi ¹, Nitul S. Rajput ², Abdellatif Bouchalkha ², Mimoun El Marssi ¹, Guillaume Matras ², Chaouki Kasmi ² and Mustapha Jouiad ^{1,*}

¹ Laboratory of Physics of Condensed Mater, University of Picardie Jules Verne, 80039 Amiens, France

² Technology Innovation Institute, Abu Dhabi P.O. Box 9639, United Arab Emirates

* Correspondence: mustapha.jouiad@u-picardie.fr

Abstract: Layered transition metals dichalcogenides such as MoS₂ and WS₂ have shown a tunable bandgap, making them highly desirable for optoelectronic applications. Here, we report on one-step chemical vapor deposited MoS₂, WS₂ and Mo_xW_{1-x}S₂ heterostructures incorporated into photoconductive devices to be examined and compared in view of their use as potential photodetectors. Vertically aligned MoS₂ nanosheets and horizontally stacked WS₂ layers, and their heterostructure form Mo_xW_{1-x}S₂, exhibit direct and indirect bandgap, respectively. To analyze these structures, various characterization methods were used to elucidate their properties including Raman spectroscopy, X-ray diffraction, X-ray photoelectron spectrometry and high-resolution transmission electron microscopy. While all the investigated samples show a photoresponse in a broad wavelength range between 400 nm and 700 nm, the vertical MoS₂ nanosheets sample exhibits the highest performances at a low bias voltage of 5 V. Our findings demonstrate a responsivity and a specific detectivity of 47.4 mA W⁻¹ and 1.4 × 10¹¹ Jones, respectively, achieved by Mo_xW_{1-x}S₂. This study offers insights into the use of a facile elaboration technique for tuning the performance of Mo_xW_{1-x}S₂ heterostructure-based photodetectors.

Keywords: photodetection; 2D materials; MoS₂; WS₂; Mo_xW_{1-x}S₂ heterostructure; CVD growth



Citation: Al Qaydi, M.; Kotbi, A.; Rajput, N.S.; Bouchalkha, A.; El Marssi, M.; Matras, G.; Kasmi, C.; Jouiad, M. Photodetection Properties of MoS₂, WS₂ and Mo_xW_{1-x}S₂ Heterostructure: A Comparative Study. *Nanomaterials* **2023**, *13*, 24. <https://doi.org/10.3390/nano13010024>

Academic Editor: Antonio Di Bartolomeo

Received: 24 November 2022

Revised: 4 December 2022

Accepted: 16 December 2022

Published: 21 December 2022



Copyright: © 2022 by the authors. Licensee MDPI, Basel, Switzerland. This article is an open access article distributed under the terms and conditions of the Creative Commons Attribution (CC BY) license (<https://creativecommons.org/licenses/by/4.0/>).

1. Introduction

Semiconductor photodetectors, namely photodiodes, are the most common types of detectors used in optical communication systems owing to their compact size, fast detection speed and high detection efficiency. Practical photodiodes can have a variety of device structures, beyond the basic PN junction construction, to improve their efficiency [1,2]. High-performance photodetectors have been used in a wide range of applications, including electro-optical displays [3], imaging [4], environmental monitoring [5], optical communication [6], military applications and security checks [7]. In these domains, two-dimensional (2D) materials, especially transition-metal dichalcogenides (TMDs), are becoming more attractive for designing photodetectors [8–10] due to their unique properties such as their ability to operate in the full range of visible light while having high photodetection polarization sensitivity, a fast photoresponse and high spatially resolved imaging [9]. This class of materials exhibits a layer-dependent electronic band structure in terms of unique physical characteristics and detection mechanisms [11,12]. Photodetectors based on 2D-TMDs materials are more sensitive throughout a wide range of the electromagnetic spectrum compared to photodetectors based on conventional bulk semiconductors [8]. However, an enhanced absorption coefficient and a longer lifespan of photoexcited carriers are preferred for optimal photocurrent generation and photodetector operation. For instance, MoS₂ thin films have a high light absorption coefficient of 10⁷ m⁻¹, a high absorption of 95% of total light [13] and a direct bandgap of 1.8 eV. Moreover, photodetectors based on 2D-TMDs possess a good current on/off ratio, efficiency,

higher chemical and mechanical stability and a stronger light–matter interaction compared to conventional photodetectors. Furthermore, mono- and few-layers MoS₂ present other desirable electronic properties that make them suitable for optoelectronic applications, such as their high carrier mobility and electrostatic integrity [14–16]. Owing to these properties, a MoS₂ single-layered transistor was found to achieve a responsivity up to $880 \times 10^3 \text{ mA W}^{-1}$ under a 560 nm excitation [17]. Moreover, an ultrabroadband multilayer MoS₂ photodetector was reported to operate in 445–2717 nm range achieving a responsivity and a specific detectivity of 50.7 mA W^{-1} and 1.6×10^9 Jones, respectively [18]. It was also shown that the photoresponse of the MoS₂ photodetector could be enhanced by chemical doping to improve its responsivity and specific detectivity up to 10^5 mA W^{-1} and 9.4×10^{12} Jones, respectively [19]. The reported responsivity and specific detectivity values are approximately 15 and 5 times higher relative to those of pristine photodetector. In addition to that, WS₂ is considered as another promising candidate for photodetection owing to a range of outstanding properties, such as its bandgap tunability, its high carrier mobility and its efficient optical absorption [20,21]. WS₂-based photodetectors have been reported to exhibit a responsivity of 4 mA W^{-1} at operating wavelengths ranging from the visible to the near infrared (IR) range [22]. Once combined with other 2D-materials such as graphene, the resulting heterostructure has shown a higher responsivity and specific detectivity of $3.5 \times 10^3 \text{ mA W}^{-1}$ and 10^{12} Jones, respectively [23]. First attempts to use a Mo_xW_{1-x}S₂ heterostructure as a photodetector showed promising performances such as a responsivity of $2.3 \times 10^3 \text{ mA W}^{-1}$ obtained under 450 nm excitation [24], and a responsivity and a specific detectivity of $6.7 \times 10^6 \text{ mA W}^{-1}$ and 3.1×10^{13} Jones under 457 nm laser light, respectively [25]. Other interesting works on alloying and ternary 2D-TMD materials can be found elsewhere [26–28].

In this work, a systematic comparative study is conducted on MoS₂, WS₂ and Mo_xW_{1-x}S₂ heterostructure to emphasize their photodetection performances while using identical fabrication and analysis routes. All samples were fabricated in one single step chemical vapor deposition (CVD) process and underwent extensive characterization investigations.

2. Materials and Methods

Among several techniques used to fabricate 2D materials, CVD is the commonly employed technique to control defects, crystallinity, and morphology of this class of materials. In particular, CVD sulfurization process is a facile one-step processing route that allows the fabrication of several sulfur based 2D-materials. The fabrication control is often ensured by monitoring several processing parameters such as gas flow, temperature, heating rate, the distance between precursors, and the position and height of the collecting substrate [29]. The synthesis of all samples was obtained in a one-step CVD process using a single-heating zone furnace at atmospheric pressure, as shown in Figure 1. The CVD system mainly consists of a quartz tube connected to high-purity (99.999%) argon cylinder streaming at flow rates of 70 sccm and 50 sccm for MoS₂ fabrication and for WS₂ and MoS₂/WS₂ respectively. The SiO₂/Si ($1 \times 1 \text{ cm}^2$) substrates were rinsed successively in deionized water, acetone, and ethanol in an ultrasonic bath for 10 min each.

A powder consisting of WO₃ ($\geq 99.8\%$), MoO₃ ($\geq 99.8\%$), or mixed WO₃/MoO₃ with ratio 1:1 was mixed with Sulphur $\geq 99.98\%$ using a ball-milling machine. All chemicals were purchased from Sigma Aldrich (Saint Louis, MO, USA). A diluted suspension solution with a concentration of 100 mg/mL was prepared using either the WO₃/S, the MoO₃/S, or the MoO₃-WO₃/S with ethanol and subsequently sonicated to enhance the homogeneity of the solution. Prior to the CVD process, a drop of 10 μL of the suspension solution was directly dropped onto the cleaned substrate using a pipette, as shown in Figure 1. Subsequently a 250 mg of sulfur powder was introduced at the edge of the sealed end of the quartz tube. Initially, the furnace was heated from room temperature up to 400 °C at a 20 °C/min heating rate, then to 850 °C at 5 °C/min for MoS₂ fabrication and 950 °C at 5 °C/min for WS₂ and MoS₂/WS₂. During the growth of either the MoS₂, the WS₂, or the

$\text{Mo}_x\text{W}_{1-x}\text{S}_2$, the temperature was maintained at 850 °C or 950 °C for 30 min. Then, the furnace was allowed to cool down naturally to room temperature.

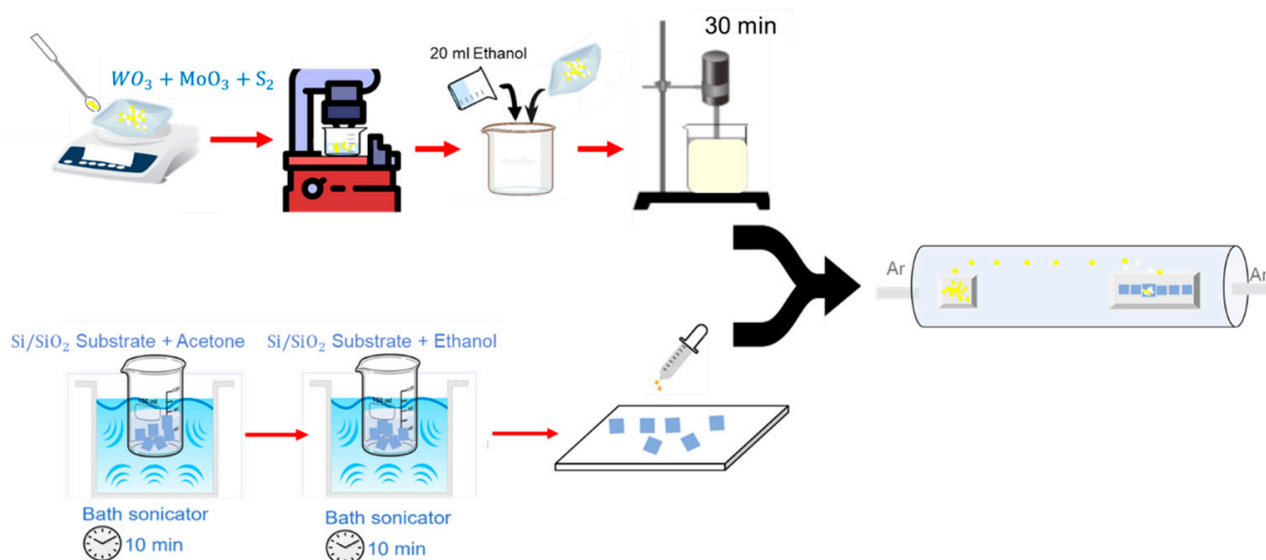


Figure 1. Fabrication protocol used for the MoS_2 , WS_2 and $\text{Mo}_x\text{W}_{1-x}\text{S}_2$ heterostructure samples.

The morphology of the fabricated specimens was analyzed using a dual beam focused-ion beam and scanning electron microscope (FIB-SEM) Scios 2 ThermoFisher Scientific (Waltham, MA, USA) microscope. The same tool was also used for the preparation of thin lamella for the transmission electron microscopy (TEM) study. TEM study was carried out using Tecnai and Titan systems from ThermoFisher Scientific (Waltham, MA, USA). TEM samples were prepared on a thin carbon coated Cu mesh grid by transferring the grown TMD samples through a gentle physical exfoliation. The vibrational modes of the processed samples were examined with a micro-Raman spectrometer Renishaw (Wotton-under-Edge, UK), using a laser excitation of 532 nm. The crystalline structure was investigated by X-ray diffraction (XRD) using a D8 Discover diffractometer Bruker (Billerica, MA, USA); $K_{\alpha\text{Cu}} = 1.54 \text{ \AA}$. The optical properties were investigated using a UV-Vis-near IR spectrometer JASCO V-670. An X-ray photoelectron spectroscopy (XPS) study was carried out using a PHI VersaProbe III scanning XPS microprobe Physical Electronics (Chanhassen, MN, USA), equipped with a monochromatic and microfocused Al K-Alpha X-ray source (1486.6 eV). During the experiment, an E-neutralizer (1 V), was implemented. CasaXPS processing software 2.3. was used for the calibration and the curve fitting. Finally, electrical measurements were performed using Palmsens-4 electrochemical workstation under ambient conditions.

3. Results and Discussion

3.1. Material Characterization

Figure 2a presents the Raman spectra of the MoS_2 sample. The observed main Raman vibrational modes indicate the presence of hexagonal 2H- MoS_2 such as E_{2g}^1 (382 cm^{-1}) and A_{1g} (409.8 cm^{-1}), which correspond to the in-plane and out-of-plane atomic vibrations, respectively [30].

The main Raman vibration modes recorded for WS_2 correspond to a 2H- WS_2 structure such as 2LA(M) , E_{2g}^1 and A_{1g} as shown in Figure 2b. The strongest peak at 350 cm^{-1} may be fitted with two sub-peaks with maximum frequencies of 323.6 cm^{-1} and 351.3 cm^{-1} leading to 2LA(M) and E_{2g}^1 , respectively. The first-order vibrational mode E_{2g}^1 represents the in-plane vibration between sulfur and tungsten atoms while the A_{1g} vibrational mode at 420 cm^{-1} corresponds to the out-of-plane vibration of sulfur atoms. It is worth noting that the A_{1g} is sensitive to the number of WS_2 layers [31].

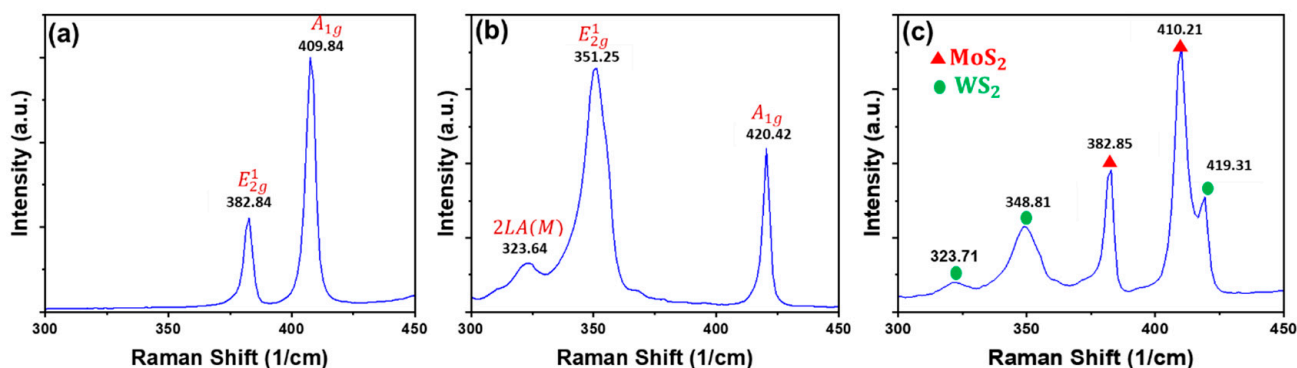


Figure 2. Vibrational modes obtained under 532 nm laser excitation for the (a) MoS₂, (b) WS₂ and (c) Mo_xW_{1-x}S₂ samples.

Regarding the Mo_xW_{1-x}S₂ heterostructure, the Raman peaks corresponding to 2H-MoS₂ and 2H-WS₂ are present, as shown in Figure 2c. The positions of the E_{2g}¹ and A_{1g} vibrational modes do not seem to shift compared to the observed peaks in individual samples. This indicates that WS₂ and MoS₂, obtained through our preparation route, have no effect on each other's long-range Coulomb interactions between the effective charges as previously reported [24].

The x-ray diffraction (XRD) diagram illustrated in Figure 3a shows clear diffraction peaks at 14.25°, 25.81°, 32.15°, 44.13° and 60.21° corresponding to 2H-MoS₂. They are attributed, respectively, to the (002), (004), (103), (006) and (008) planes of the hexagonal 2H-MoS₂. For WS₂, the XRD diagram shows several significant diffraction peaks at 14.3°, 28.8°, 43.9°, 59.8°, and 77.13° as can be seen in Figure 3b. They are attributed to 2H-WS₂ planes (002), (004), (006), (008) and (00,10).

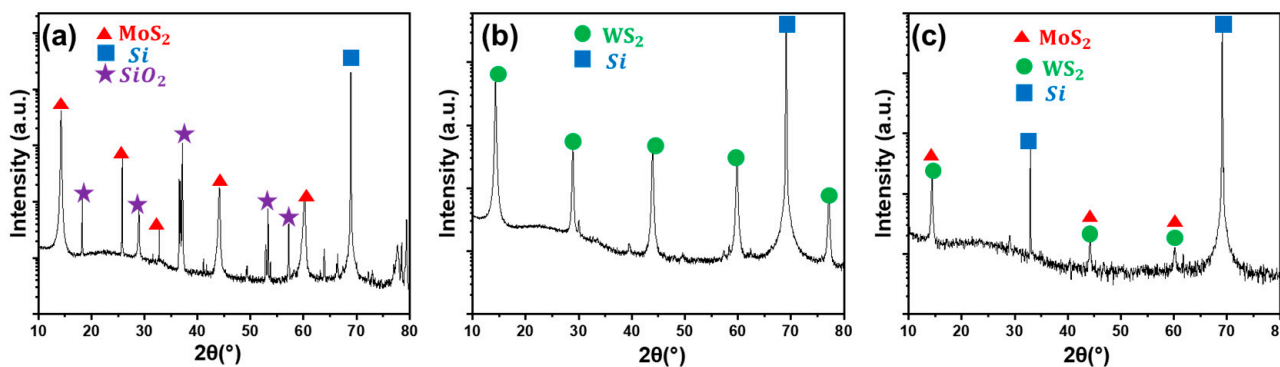


Figure 3. XRD diagrams recorded for the as-grown (a) MoS₂, (b) WS₂ and (c) Mo_xW_{1-x}S₂.

For the Mo_xW_{1-x}S₂ heterostructure, the MoS₂ and WS₂ peaks are present in the corresponding XRD diagram given in Figure 3c. This confirms the successful fabrication of the heterostructure. The sharp diffraction peaks observed on the spectra are a clear indication of the high crystallinity of the fabricated nanosheets.

The SEM images show different morphologies for the MoS₂, WS₂ and the heterostructure samples. The MoS₂ flakes (Figure 4a) are observed to grow vertically. This is highlighted at a higher magnification in Figure 4b. Similar results were reported previously [32]. On the other hand, WS₂ shows accumulated crystals stacked on top of the substrate. A large number of triangular shaped flakes disposed horizontally are visible in Figure 4c,d at low and high magnifications, respectively.

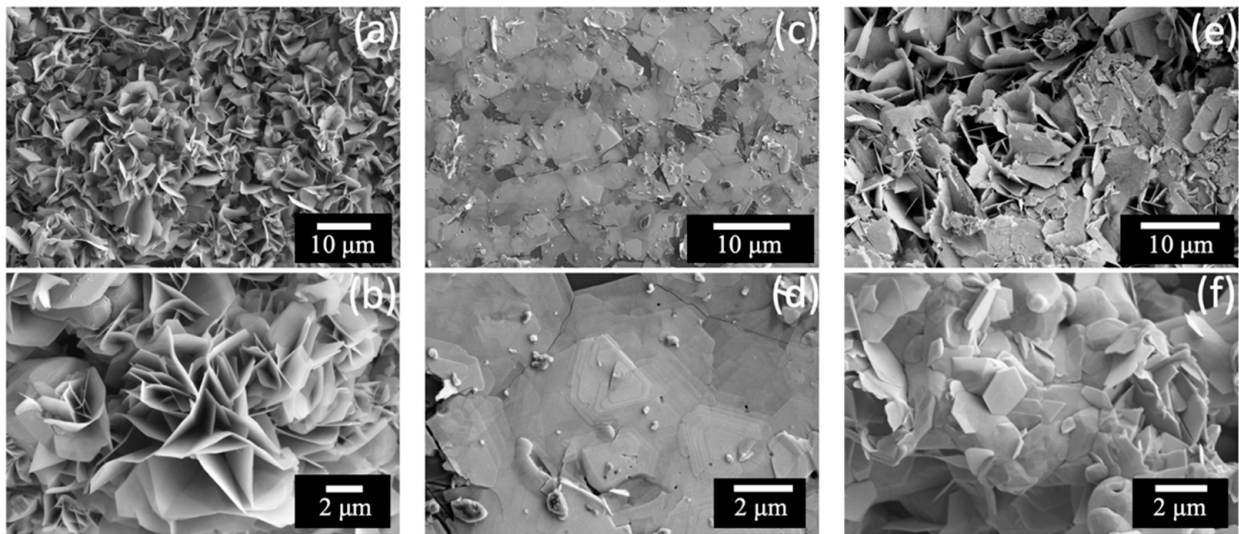


Figure 4. Low and high magnification SEM images of (a,b) MoS₂ vertically aligned nanosheets (c,d) WS₂ stacked layers and (e,f) Mo_xW_{1-x}S₂ co-existent vertical and stacked layers.

As can be seen in Figure 4e,f, the Mo_xW_{1-x}S₂ heterostructure exhibits a mixed morphology. It consists of both vertically aligned MoS₂ nanosheets and stacked layers of WS₂. A coherence between the two phases is observed with no visible segregation between the two compounds.

The change in the MoS₂ and WS₂ morphology could be attributed to the following hypotheses: (1) The high CVD reaction temperature used to process the WS₂ could enhance the nucleation kinetics of the first WS₂ seeds allowing the coalescence process to occur horizontally. In contrast, for MoS₂ the reaction temperature is lower leading to dispersed seeds in the surface of the substrate favoring the coalescence on the top of the first layers; (2) The WS₂ weight may impede the vertical shape of WS₂; (3) The flow rate used for the processing of WS₂ (50 sscm) is lower compared to the one for MoS₂ fabrication (70 sscm), which may not allow the evacuation of sulfur excess.

In order to comprehend the mixing mechanism of MoS₂ and WS₂ structures, we have conducted further microstructure analysis using HRTEM for the three samples as shown in Figure 5.

Figure 5a shows a TEM cross-sectional view of the vertically oriented MoS₂ nanosheets (thickness ~100 nm). Higher resolution imaging (Figure 5b) indicates an interplanar spacing of 2H-MoS₂ of ~0.62 nm. Moreover, Figure 5c depicts the base region at the interface between the MoS₂ and the substrate, showing the nucleation of the 2H-MoS₂. The zoomed view in Figure 5c indicates the nature of the flakes' growth, where certain layers tend to be continuous and few sheets get terminated due to the absence of growth space, which could be at the origin of the vertically aligned 2H-MoS₂. Figure 5e–g shows the cross-sectional views of the WS₂ sample. The smooth planar growth of the WS₂ is clearly visible compared to MoS₂, in agreement with the observation on the SEM images. An interplanar distance of 2H-WS₂ is determined at ~0.65 nm. Figure 5h shows typical TEM bright field images obtained from the Mo_xW_{1-x}S₂ heterostructure showing an overlapping region (red and purple boxes). Zoomed images of both boxes indicate the presence of 2H-MoS₂ (red box, Figure 5i) and 2H-WS₂ (purple box, Figure 5j), which is a signature of the MoS₂-WS₂ heterostructure form with a crystallographic relationship (200)_{MoS₂}//(101)_{WS₂}. Moreover, it is worth noting that 2D materials in their single-phase form are often considered to be thermally stable. Nevertheless, in their heterostructure form, they may suffer from thermal defects and induced stresses that could affect their electronic and optical properties. In the current work, these inherent stresses have not been evaluated as well as their impact on the heterostructure physical properties. It is believed that the effects of these stresses on the heterostructure structural and electronic properties cannot be neglected.

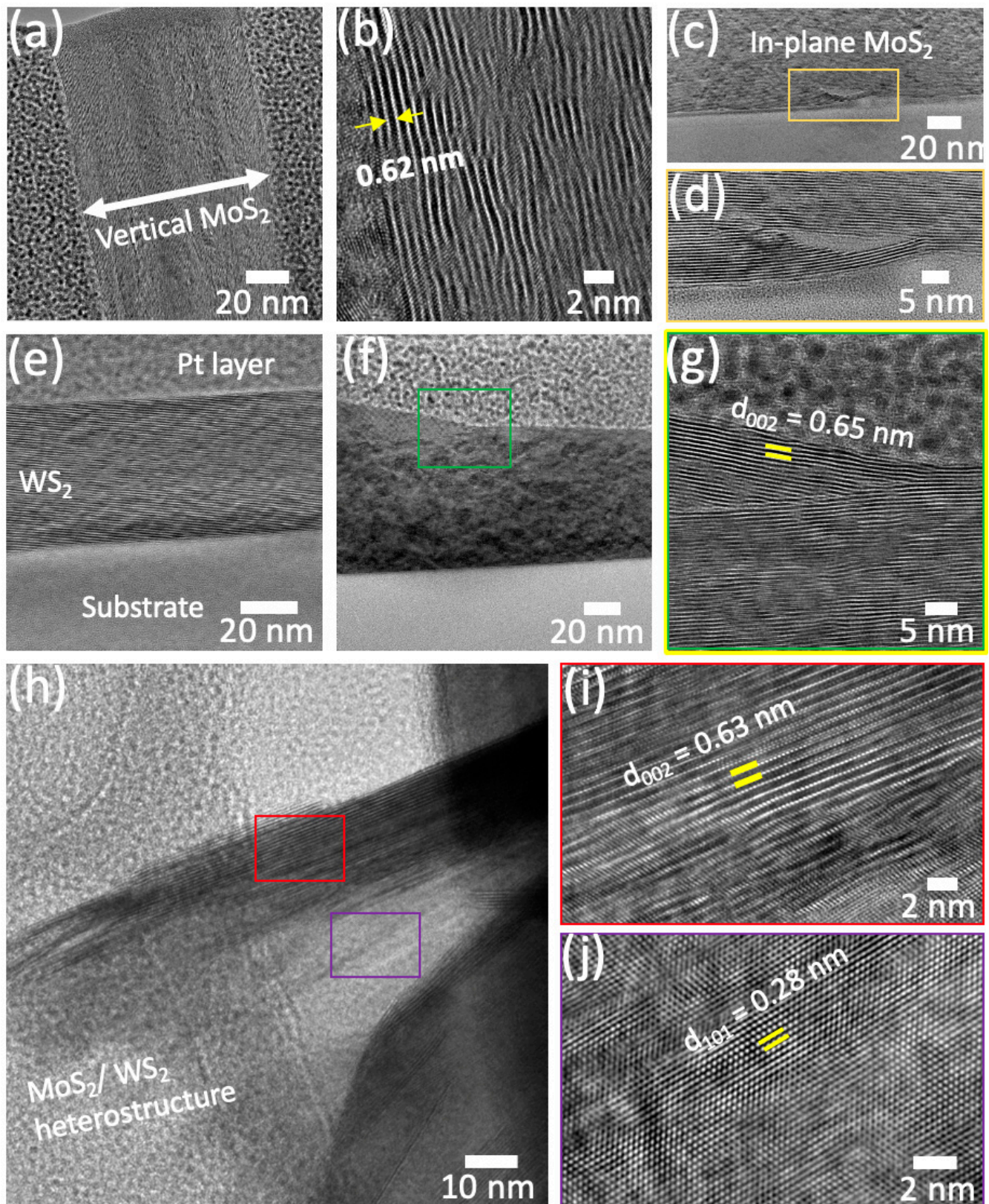


Figure 5. Typical TEM microstructure at low and high magnifications. (a,b) Cross-sectional bright field TEM images of vertically oriented MoS₂ flakes; (c,d) TEM image of in-plane MoS₂; (e–g) cross-sectional views of deposited multi-stacked WS₂ layers; (h–j) bright-field image of the Mo_xW_{1-x}S₂ heterostructure.

To precisely investigate the chemical composition of the fabricated samples, we have conducted XPS analyses, as shown in Figure 6.

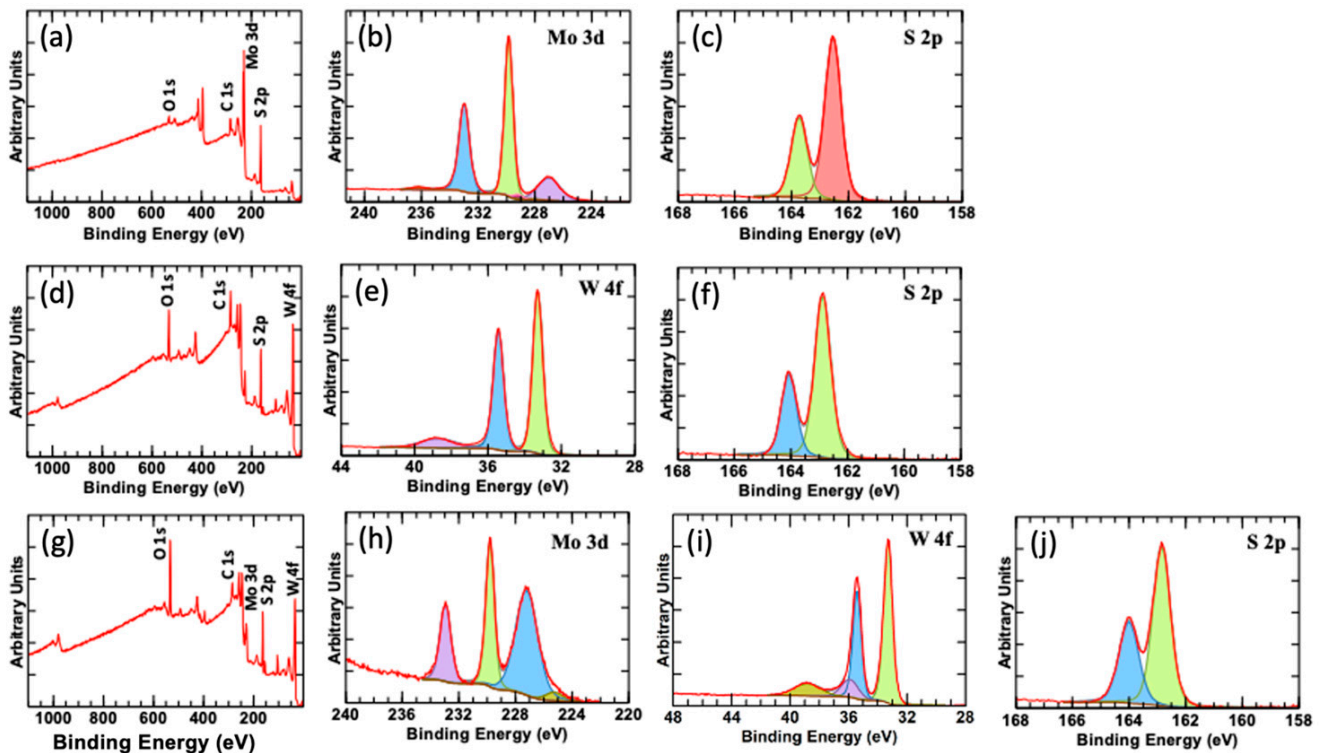


Figure 6. XPS analyses for the (a–c) MoS₂, (d–f) WS₂ and (g–j) Mo_xW_{1-x}S₂ samples.

The XPS survey scan of the MoS₂ sample, shown in Figure 6a, indicates the presence of MoS₂ constituting elements. This figure shows strong peaks for Mo 3d and S 2p orbitals. The peak at 227.02 eV corresponds to the S 2s peak. The two strong peaks at 229.85 eV and 232.99 eV are attributed to Mo⁴⁺ 3d_{5/2} and 3d_{3/2} (Figure 6b). A small peak appearing at 236.2 eV indicates a minor oxidation of the Mo material [33]. For Sulfur, S 2p peaks are recorded and shown in Figure 6c. The two strong peaks at 162.54 eV and 163.73 eV are attributed to S²⁻ 2p_{3/2} and p_{1/2} states. Regarding the WS₂, the XPS survey scan (Figure 6d) indicates the presence of W and S in the material, translated by the strong peaks for W 4f_{7/2} and W 4f_{5/2} appearing at 33.28 eV and 35.43 eV, respectively (Figure 6e). An additional peak appears at 38.72 eV that could be attributed to W p_{3/2}. The S peaks appearing at 162.88 eV and 164.07 eV are due to the S²⁻ 2p_{3/2} and p_{1/2} states, respectively (Figure 6f). Moreover, the XPS survey scan obtained from the Mo_xW_{1-x}S₂ heterostructure sample is provided in Figure 6g, indicating the presence of W, Mo, and S in the heterostructure. The Mo 3d peaks are found at 229.79 eV and 232.95 eV (Figure 6h), and the S 2s peak is found at 227.2 eV. Additionally, strong peaks of W appear at 33.3 eV and 35.42 eV, corresponding to W 4f_{7/2} and W 4f_{5/2}. The peak at 35.91 eV could be attributed to W-O bond, while the 38.80 eV peak is attributed to W 5p_{3/2} (Figure 6i). The S peaks appearing at 162.84 eV and 164.0 eV correspond to the S²⁻ 2p_{3/2} and p_{1/2} states, respectively (Figure 6j).

3.2. Optical Properties

Density functional theory (DFT) calculations, using generalized gradient approximation (GGA) and Perdew Burke Ernzerhof (PBE) methods (implemented in Quantum Espresso) were first used to estimate the structural optimizations and electronic attributes (see Supplementary Materials). We have summarized in Table 1 the crystal structures of MoS₂ and WS₂, as well as the cell parameters, the cutoff wave function and charge densities for both materials implemented in DFT calculations. For all configurations (monolayer and

bilayer), the cell parameters and atomic locations were fully relaxed using the Broyden-Fletcher-Goldfarb-Shanno (BFGS) approach until the remaining force on each atom was less than 10^{-3} Ryd/Bohr (see Supplementary Materials).

Table 1. Crystal systems, cut off wave function and cell parameters implemented in DFT calculations.

Material	Crystal System	Cut Off/ Wave Function (Ryd)	Lattice Parameters (Å)
MoS ₂	P63/mmc	70/700	a = b = 3.18; c = 15
WS ₂	P63/mmc	50/500	a = b = 3.19; c = 15
Mo _x W _{1-x} S ₂	P63/mmc	60/600	a = b = 3.18; c = 15

To simulate monolayers in our calculations, a vacuum space of 15 Å was created along both sides of the z-axis to isolate the crystal and prevent interactions between the adjacent layers. For the sampling of the Brillouin zone, a Monkhorst-Pack technique is used, with k-point meshes of $9 \times 9 \times 2$ for the bulk and $9 \times 9 \times 1$ for the monolayer and bilayer structures. The generated optimal structure was utilized to compute the band structures for various setups. The results revealed a transition from an indirect bandgap to a direct bandgap as the structure changed from bulk to monolayer for both WS₂ and MoS₂. Similar results have been reported [29,34–36]. The band structure of the MoS₂ and WS₂ layers were well conserved, as seen in Figure 7.

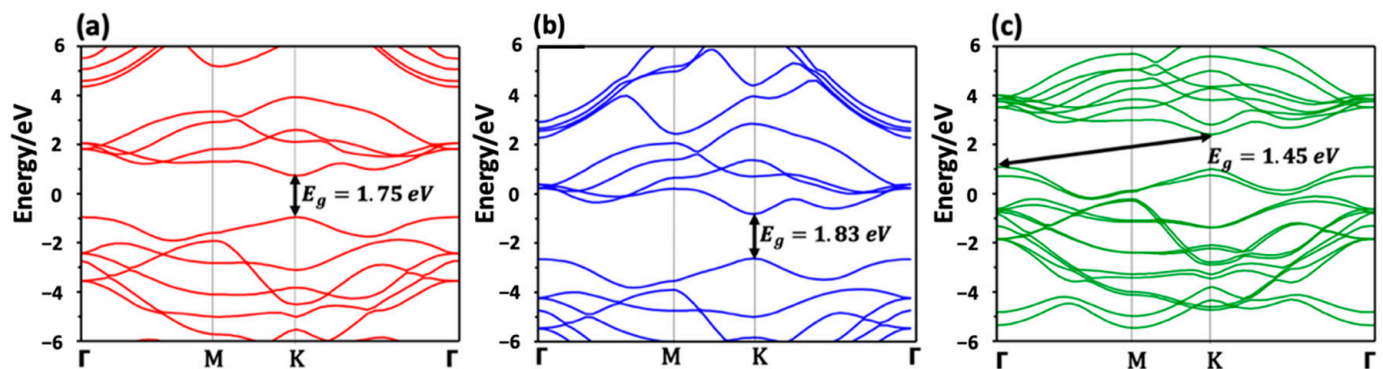


Figure 7. DFT computed electronic bands structure for monolayer (a) MoS₂, (b) WS₂ and (c) Mo_xW_{1-x}S₂.

The conduction band minimum (CB_{min}) and the valence band maximum (VB_{min}) of the MoS₂ and WS₂ monolayers are positioned at the K point, respectively. Mo_xW_{1-x}S₂ is an indirect semiconductor with a 1.45 eV indirect bandgap. Unlike their homogeneous bilayers' counterparts, the CB_{min} of Mo_xW_{1-x}S₂ heterostructures is positioned at the K point, whilst the VB_{min} is located at the point Γ. Through van der Waals interactions, the MoS₂ and WS₂ monolayers produce an atomically sharp type-II heterointerface, which may be favorable for electron–hole pair separation. Free electrons and holes will spontaneously separate in a type II heterostructure, which is useful for optoelectronics and solar energy conversion applications [37–39].

Furthermore, the optical reflectance of all samples was measured at room temperature in the wavelength range 400–800 nm as shown in Figure 8a.

MoS₂ shows the lowest reflectance compared to the other samples, with the presence of both excitons, A and B, clearly visible at 636 nm and 688 nm positions, respectively [40,41]. This is due to the high optical absorption of the vertical morphology of the MoS₂ nanosheets with high specific area and light trapping via the multiple scattering effects [42]. On the other hand, WS₂ exciton appears clearly at 620 nm, showing the highest reflectance caused by its planar morphology. Finally, the reflectance of the Mo_xW_{1-x}S₂ sample shows a mixed behavior between MoS₂ and WS₂ with an enhancement of the MoS₂ excitons. This validates

the successful fabrication of the heterostructure as confirmed by the Raman spectroscopy and HRTEM analyses discussed earlier.

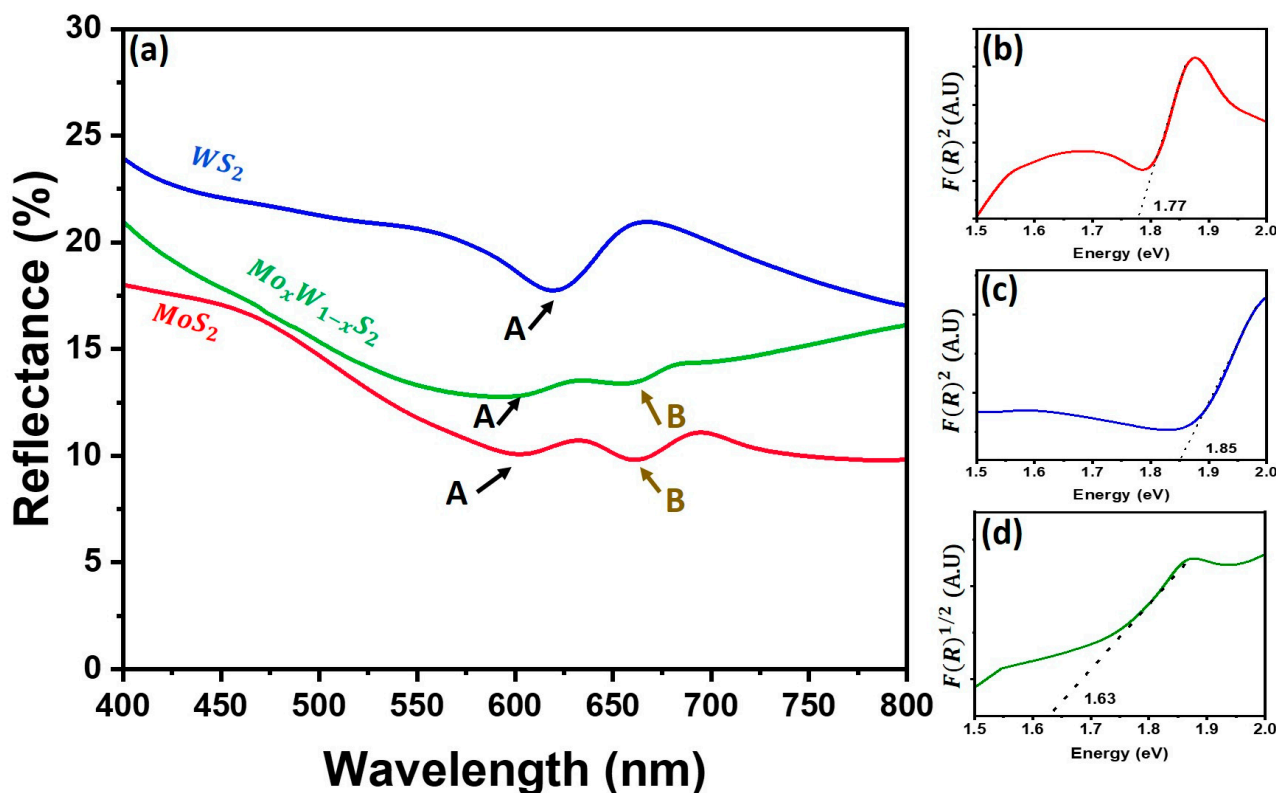


Figure 8. Reflectance for all samples (a) (red: MoS₂; blue: WS₂ and green: Mo_xW_{1-x}S₂). The insets (b–d) show the variation of the reflectance function versus energy determined by the Kubelka-Munk model. The respective bandgap energies are indicated by dashed lines.

To obtain the optical bandgap, the reflectance measurements recorded for all investigated samples are implemented in Kubelka-Munk model as per the following equation [43]:

$$F(R) = \frac{K}{S} = \frac{(1-R)^2}{2R} \quad (1)$$

where K represents the molar absorption coefficient, S is the scattering factor, and R is the reflectance. Our results show that both MoS₂ and WS₂ exhibit a bandgap of 1.77 eV and 1.85 eV, respectively, approximately equivalent to bandgap obtained using DFT calculations. In contrast, the Mo_xW_{1-x}S₂ sample shows a low bandgap of 1.63 eV compared to DFT calculations, which is probably due to the heterostructure construction and implementation in DFT that does not seem to reproduce the effective form of the heterostructure.

3.3. Photoresponse Measurements

To evaluate the optoelectronic properties of the MoS₂, WS₂, and Mo_xW_{1-x}S₂ nanocomposite films, we deposited a pair of Au electrodes onto the device surface, as illustrated in Figure 9. The electrical measurements were conducted at room temperature under dark and illumination conditions using a halogen lamp (70 mW/cm²), and under different excitation wavelengths ranging from 400 nm to 700 nm. The effective detection area of the samples was 0.075 cm².

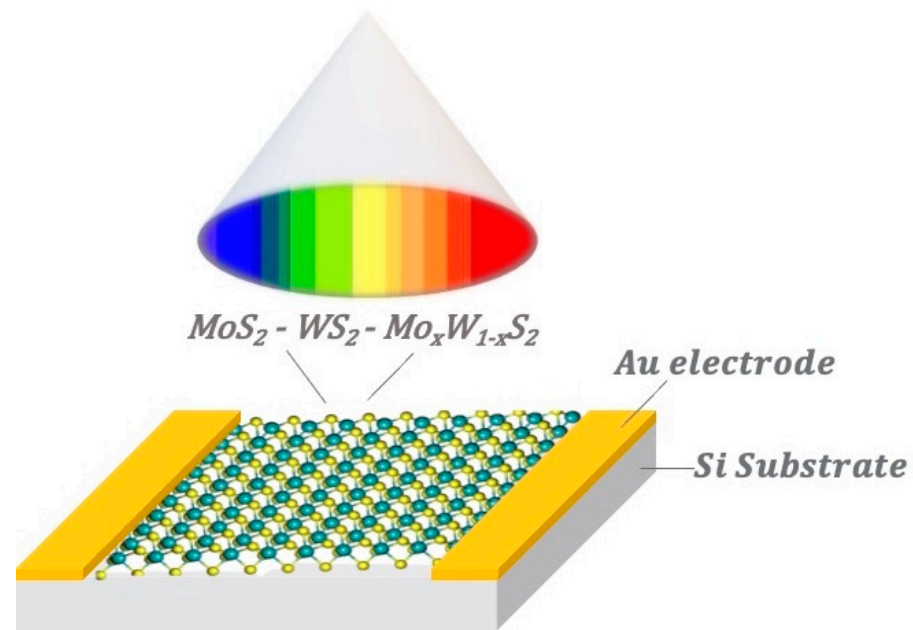


Figure 9. Schematic of the photoresponse measurements set up used for all samples.

The J-V curves were collected using a voltage sweep program $-/+ 5$ V at 0.1 V step. The J_{ph} at 5 V bias was subsequently computed using the following formula:

$$J_{ph} \left(mA/cm^2 \right) = \frac{I_{light} - I_{dark}}{A} \quad (2)$$

where I_{light} and I_{dark} represent the current obtained in the light and the dark conditions, respectively. A is the active detection area.

The photoresponse (P) of our samples was computed using the following equation:

$$P(\%) = 100 \frac{I_{light} - I_{dark}}{I_{dark}} \quad (3)$$

The responsivity (R_λ) and the relative detectivity (D^*) [17] of the photodetectors were obtained using the following equations:

$$R_\lambda = \frac{I_{ph}}{P_{light}} \quad (4)$$

$$D^* = \frac{R_\lambda}{(2qI_{dark})^{\frac{1}{2}}} \quad (5)$$

where q is the absolute value of an electron charge (1.6×10^{-19} Coulombs), R_λ is the responsivity given in units of $mA W^{-1}$, and D^* is the relative detectivity given in units of Jones.

In Figure 10, compared to the other samples, MoS_2 exhibits the highest J_{ph} achieving $4.8 mA/cm^2$, compared to the other samples, while WS_2 and the heterostructure $Mo_xW_{1-x}S_2$ have shown lower values of $0.8 mA/cm^2$ and $3.7 mA/cm^2$, respectively. Moreover, the highest photoresponse is also achieved by $MoS_2 \sim 6.8 \times 10^4\%$, while WS_2 exhibits the lowest one of $1.5 \times 10^3\%$. The photoresponse of $Mo_xW_{1-x}S_2$ heterostructure of $\sim 5.8 \times 10^3\%$ is similar to previously reported values [44]. This strong photoresponse is due to the high optical absorbance of the vertical MoS_2 nanosheets, known for possessing a high ability to capture light and a quick charge transfer [45] (e.g., Figure 10a–c).

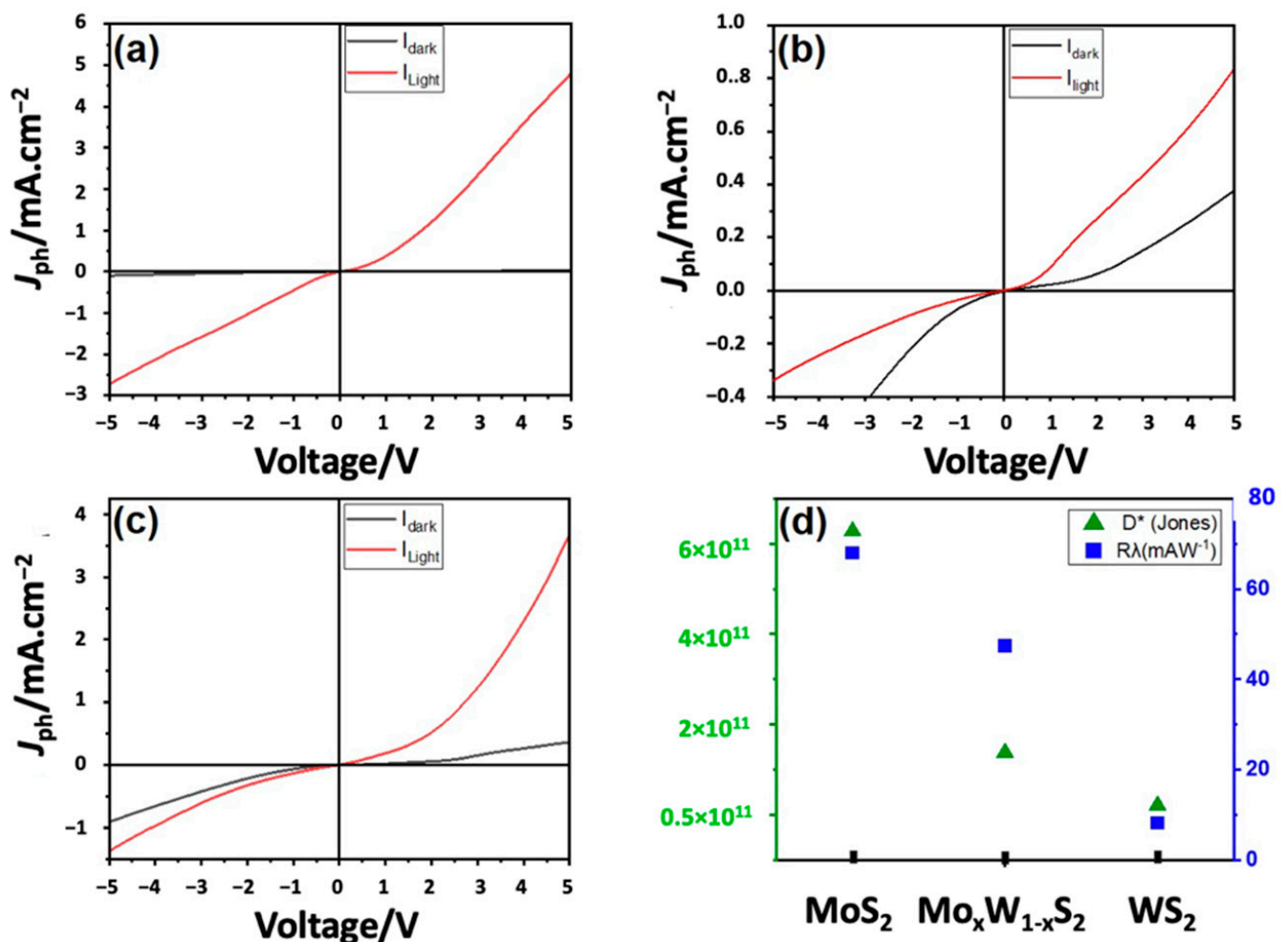


Figure 10. (a) Photocurrent density measurements for (a) MoS₂, (b) WS₂, (c) Mo_xW_{1-x}S₂, and their respective (d) responsivity and relative detectivity obtained under halogen lamp illumination (70 mW/cm²).

For MoS₂, we obtain maximum values of R_λ and D^* , respectively at 68 mA W⁻¹ and 6.3×10^3 Jones, with a 5 V bias voltage. It is worth noting that higher R_λ values were also reported [18,19,46,47], however in those works the considered active area was extremely smaller ($\sim 10^{-7}$ cm²) and a high applied bias was considerably higher (~ 50 V) compared to our present study. Instead, our findings concur that WS₂ and Mo_xW_{1-x}S₂ heterostructure exhibit R_λ and D^* of 8.9 mA W⁻¹, 2.1×10^{10} Jones and 47.4 mA W⁻¹, 1.4×10^{11} Jones, respectively compared to MoS₂.

For further examinations of the photoresponse of our samples, we conducted a series of photoresponse measurements under monochromatic light excitations in the range between 400 nm and 700 nm wavelengths. Figure 11d shows the relative detectivity D^* computed at various wavelengths using the above-mentioned formula (Equations (4) and (5)), which is in agreement with the measured values in Figure 10d. From the latter, one can notice that R_λ and D^* are decreasing from 77.2 to 10.9 mA W⁻¹ and from 7.2×10^{11} to 1.8×10^{10} Jones, respectively, with an increasing excitation wavelength from 400 nm to 700 nm.

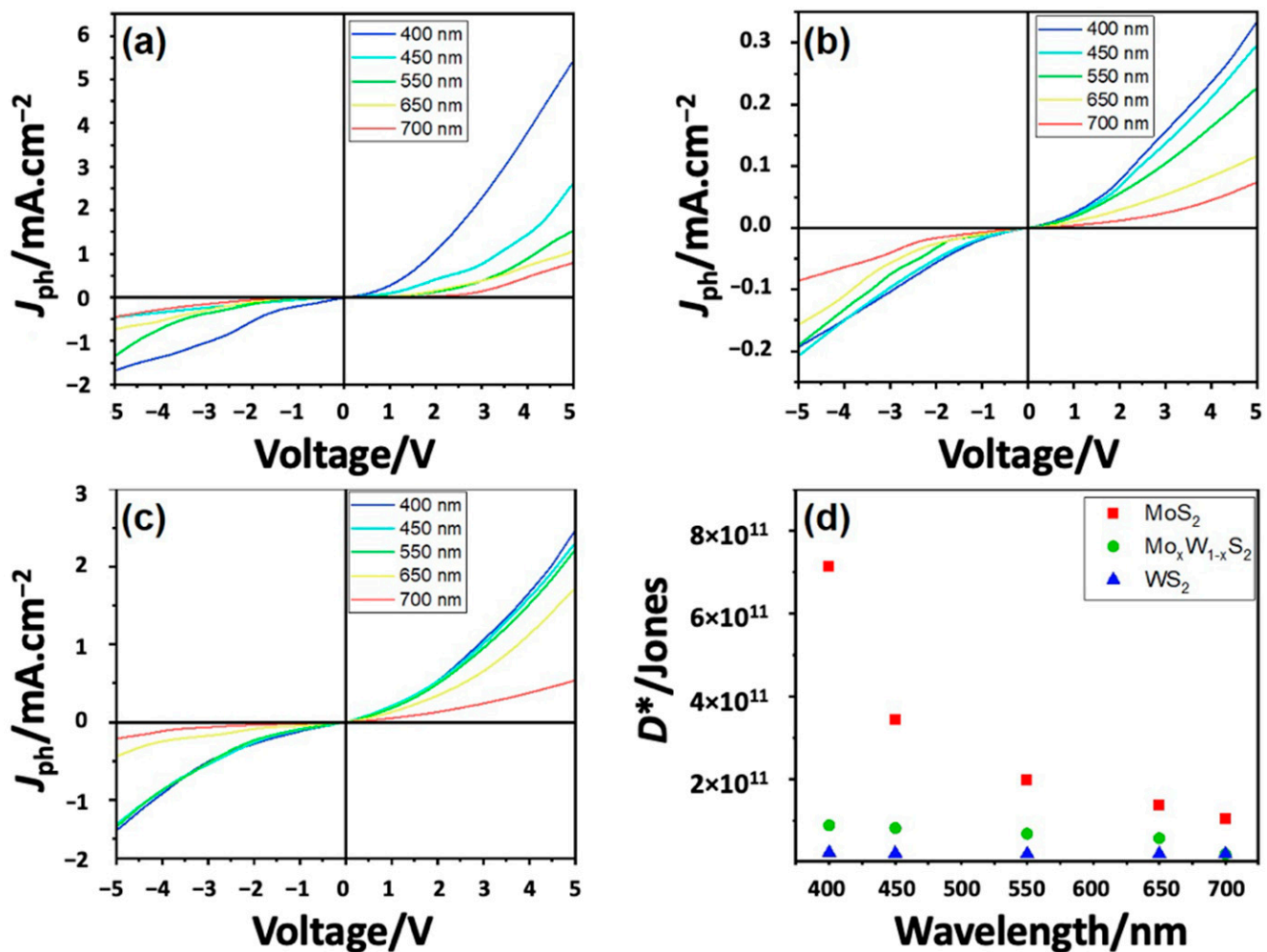


Figure 11. Photocurrent density J_{ph} measured for (a) MoS₂, (b) WS₂, (c) Mo_xW_{1-x}S₂, and (d) their respective relative detectivity under 400–700 nm wavelength excitations.

The maximum responsivity R_λ of 77.2 mA W^{-1} and the relative detectivity D^* of 7.2×10^{11} Jones, were obtained at 400 nm excitation for MoS₂ sample as reported elsewhere [18,19,46,47].

To further correlate our investigation with existing works, we conducted a survey of available data for sole MoS₂, WS₂ and the heterostructure made out of these compounds. The survey is summarized in Table 2.

The photodetection obtained for MoS₂ shows similar performances in terms of detectivity with slightly better performance of our CVD-fabricated MoS₂ compared to the sample processed by PLD. However, there is a difference in responsivity, mainly attributed to applied high bias voltages ($\sim 50 \text{ V}$) and very low active area used 10^{-7} cm^2 , compared to our active area of 10^{-2} cm^2 . This shows that our one-step fabricated MoS₂ has exhibited high photodetection performances despite the larger effective area used. To the best of our knowledge, no previous results were reported on WS₂ better than our results on CVD-grown samples achieving a responsivity of 11.8 mA W^{-1} and a detectivity of 10^{10} Jones, obtained at a very low bias voltage of 5 V. The control of CVD parameters to grow a high quality Mo_xW_{1-x}S₂ monolayer was already reported [28]. Similarly, we have fabricated the Mo_xW_{1-x}S₂ using a one-step CVD fabrication method achieving a responsivity and a detectivity of 47 mA W^{-1} and 10^{11} Jones, respectively. Similar results were reported before using a mixture of MoS₂/WS₂ monolayers and graphene or using MoS₂ core shell containing WS₂. We believe that our results indicate that our processing route consisting of

a one-step and low-cost CVD fabrication technique of MoS₂, WS₂ and Mo_xW_{1-x}S₂ hold a strong promising potential for the future development of scalable photodetector devices.

Table 2. Photodetection performances of our samples with respect to the literature.

Material	Fabrication	Bias (V)	Power Density (mW cm ⁻²)	Active Area (cm ²)	Excitation (nm)	Responsivity (mA W ⁻¹)	Detectivity (Jones)	Ref.
MoS ₂	PLD	10	8	1.2 × 10 ⁻³	445–2717	50.7	1.55 × 10 ⁹	[18]
MoS ₂ -HfO ₂	Exfoliation	5	-	1.5 × 10 ⁻⁷	550–800	104	7.7 × 10 ¹¹	[45]
MoS ₂ /GaN substrate	CVD	20	2.9	4.7 × 10 ⁻⁴	460	25 × 10 ³	5.6 × 10 ⁸	[47]
MoS ₂ /Graphene	CVD	10	1	6 × 10 ⁻⁶	532–633	1.4 × 10 ³	8.7 × 10 ¹⁴	[48]
MoS ₂	CVD	50	7	6.8 × 10 ⁻⁷	450–750	105	9.4 × 10 ¹²	[19]
MoS ₂	CVD	5	70	7.5 × 10 ⁻²	400–700	77.2	7.2 × 10 ¹¹	[This study]
WS ₂	Sputtering	10	14.9	9 × 10 ⁻⁷	450–635	0.4	4.4 × 10 ⁶	[49]
WS ₂	Sputtering	5	-	-	365	53.3 × 10 ³	1.22 × 10 ¹¹	[50]
WS ₂ -Graphene	CVD	5	2.5 × 10 ⁷	4 × 10 ⁻¹²	532	3.5 × 10 ³	1.6 × 10 ¹⁰	[23]
WS ₂	Exfoliation	5	11.7	-	532–1064	4.1	2.6 × 10 ⁹	[22]
WS ₂	CVD	10	0.07	1.7 × 10 ⁻⁶	532	0.5	4.9 × 10 ⁹	[51]
WS ₂	CVD	5	70	7.5 × 10 ⁻²	400–700	11.8	2.9 × 10 ¹⁰	[This study]
MoS ₂ /WS ₂ Graphene	CVD	10	1.7 × 10 ²	3.1 × 10 ⁻⁸	532	2340 × 10 ³	4.1 × 10 ¹¹	[44]
MoS ₂ /WS ₂	2-steps CVD	4	-	1.2 × 10 ⁻⁵	450	2.3 × 10 ³	-	[24]
WS ₂ /MoS ₂	2-steps CVD	5	1.3 × 10 ³	6.2 × 10 ⁻⁷	457–671	6.7 × 10 ³	3.1 × 10 ¹³	[25]
Mo _x W _{1-x} S ₂	CVD	5	70	7.5 × 10 ⁻²	400–700	47.4	1.4 × 10 ¹¹	[This study]

4. Conclusions

A Mo_xW_{1-x}S₂ heterostructure was successfully synthesized by a one-step CVD route. The high purity and high quality of the samples have been confirmed by multiple characterization techniques. The incorporation of the MoS₂, WS₂ and the Mo_xW_{1-x}S₂ heterostructure into photoconductive devices demonstrated a promising potential of these compounds to be used as broadband photodetectors. In particular, the Mo_xW_{1-x}S₂ heterostructure has achieved a responsivity of 47.4 mA W⁻¹ and a relative detectivity of 1.4 × 10¹¹ Jones under visible light excitation ranging from 400 to 700 nm.

Supplementary Materials: The following supporting information can be downloaded at: <https://www.mdpi.com/article/10.3390/nano13010024/s1>, Figure S1: Crystals configuration used in DFT for (a) MoS₂, (b) WS₂ and (c) Mo_xW_{1-x}S₂; Figure S2: Bandgap computed by DFT simulations (a) direct bandgap for monolayer MoS₂, (b) indirect bandgap for bilayer MoS₂; Figure S3: Bandgap obtained using Kubelka-Munck model (a) direct bandgap for monolayer MoS₂, (b) indirect bandgap for bilayer MoS₂; Figure S4: Bandgap computed using DFT simulations (a) direct bandgap for monolayer WS₂, (b) indirect bandgap for bilayer WS₂; Figure S5: Bandgap obtained using Kubelka-Munck model (a) direct bandgap for monolayer WS₂, (b) indirect bandgap for bilayer WS₂.

Author Contributions: M.A.Q. and M.J. conceived the study; M.A.Q., N.S.R. and A.K. carried out the experimental and theoretical investigations; M.A.Q., A.K., M.E.M., G.M., C.K., A.B. and M.J. analyzed the data. All authors contributed equally on writing, editing and reviewing the manuscript. All authors have read and agreed to the published version of the manuscript.

Funding: Authors acknowledge the financial support from Technology Innovation Institute under grant number TII/DERC/2091/2020 (Ref. UPJV-2021-DR-83).

Data Availability Statement: Data would be made available upon request to the corresponding author.

Acknowledgments: This work is a research collaboration between the University of Picardie Jules Verne (UPJV), France and Technology Innovation Institute (TII), UAE.

Conflicts of Interest: The authors declare no conflict of interest.

References

- Hui, R. Photodetectors. In *Introduction to Fiber-Optic Communications*; Elsevier: Amsterdam, The Netherlands, 2020; pp. 125–154.
- Malik, M.; Iqbal, M.A.; Choi, J.R.; Pham, P.V. 2D Materials for Efficient Photodetection: Overview, Mechanisms, Performance and UV-IR Range Applications. *Front. Chem.* **2022**, *10*, 905404. [[CrossRef](#)] [[PubMed](#)]
- Sciuto, A.; Roccaforte, F.; Raineri, V. Electro-Optical Response of Ion-Irradiated 4H-SiC Schottky Ultraviolet Photodetectors. *Appl. Phys. Lett.* **2008**, *92*, 093505. [[CrossRef](#)]
- Li, L.; Chen, H.; Fang, Z.; Meng, X.; Zuo, C.; Lv, M.; Tian, Y.; Fang, Y.; Xiao, Z.; Shan, C.; et al. An Electrically Modulated Single-Color/Dual-Color Imaging Photodetector. *Adv. Mater.* **2020**, *32*, 1907257. [[CrossRef](#)] [[PubMed](#)]
- Tyagi, D.; Wang, H.; Huang, W.; Hu, L.; Tang, Y.; Guo, Z.; Ouyang, Z.; Zhang, H. Recent Advances in Two-Dimensional-Material-Based Sensing Technology toward Health and Environmental Monitoring Applications. *Nanoscale* **2020**, *12*, 3535–3559. [[CrossRef](#)] [[PubMed](#)]
- Arams, F.R. Photodetectors for Optical Communication Systems. *Proc. IEEE* **1970**, *58*, 1466–1486. [[CrossRef](#)]
- Rogalski, A.; Antoszewski, J.; Faraone, L. Third-Generation Infrared Photodetector Arrays. *J. Appl. Phys.* **2009**, *105*, 4. [[CrossRef](#)]
- Xi, F.; Wang, H.; Xiao, D.; Dubey, M.; Ramasubramaniam, A. Two-Dimensional Material Nanophotonics. *Nat. Photonics* **2010**, *4*, 882. [[CrossRef](#)]
- Wang, L.; Meric, I.; Huang, P.Y.; Gao, Q.; Gao, Y.; Tran, H.; Taniguchi, T.; Watanabe, K.; Campos, L.M.; Muller, D.A.; et al. One-Dimensional Electrical Contact to a Two-Dimensional Material. *Science* **2013**, *342*, 614–617. [[CrossRef](#)]
- Koski, K.J.; Cui, Y. The New Skinny in Two-Dimensional Nanomaterials. *ACS Nano* **2013**, *7*, 3739–3743. [[CrossRef](#)]
- Wang, Q.H.; Kalantar-Zadeh, K.; Kis, A.; Coleman, J.N.; Strano, M.S. Electronics and Optoelectronics of Two-Dimensional Transition Metal Dichalcogenides. *Nat. Nanotechnol.* **2012**, *7*, 699–712. [[CrossRef](#)]
- Radisavljevic, B.; Radenovic, A.; Brivio, J.; Giacometti, V.; Kis, A. Single-Layer MoS₂ Transistors. *Nat. Nanotechnol.* **2011**, *6*, 147–150. [[CrossRef](#)] [[PubMed](#)]
- Lee, E.W.; Lee, C.H.; Paul, P.K.; Ma, L.; McCulloch, W.D.; Krishnamoorthy, S.; Wu, Y.; Arehart, A.R.; Rajan, S. Layer-Transferred MoS₂/GaN PN Diodes. *Appl. Phys. Lett.* **2015**, *107*, 103505. [[CrossRef](#)]
- Splendiani, A.; Sun, L.; Zhang, Y.; Li, T.; Kim, J.; Chim, C.Y.; Galli, G.; Wang, F. Emerging Photoluminescence in Monolayer MoS₂. *Nano Lett.* **2010**, *10*, 1271–1275. [[CrossRef](#)] [[PubMed](#)]
- Ponomarev, E.; Gutiérrez-Lezama, I.; Ubrig, N.; Morpurgo, A.F. Ambipolar Light-Emitting Transistors on Chemical Vapor Deposited Monolayer MoS₂. *Nano Lett.* **2015**, *15*, 8289–8294. [[CrossRef](#)]
- George, A.; Fistul, M.V.; Gruenewald, M.; Kaiser, D.; Lehnert, T.; Mupparapu, R.; Neumann, C.; Hübner, U.; Schaal, M.; Masurkar, N.; et al. Giant Persistent Photoconductivity in Monolayer MoS₂ Field-Effect Transistors. *npj 2D Mater. Appl.* **2021**, *5*, 15. [[CrossRef](#)]
- Lopez-Sanchez, O.; Lembke, D.; Kayci, M.; Radenovic, A.; Kis, A. Ultrasensitive Photodetectors Based on Monolayer MoS₂. *Nat. Nanotechnol.* **2013**, *8*, 497–501. [[CrossRef](#)]
- Xie, Y.; Zhang, B.; Wang, S.; Wang, D.; Wang, A.; Wang, Z.; Yu, H.; Zhang, H.; Chen, Y.; Zhao, M.; et al. Ultrabroadband MoS₂ Photodetector with Spectral Response from 445 to 2717 Nm. *Adv. Mater.* **2017**, *29*, 1605972. [[CrossRef](#)]
- Li, S.; Chen, X.; Liu, F.; Chen, Y.; Liu, B.; Deng, W.; An, B.; Chu, F.; Zhang, G.; Li, S.; et al. Enhanced Performance of a CVD MoS₂ Photodetector by Chemical in Situ N-Type Doping. *ACS Appl. Mater. Interfaces* **2019**, *11*, 11636–11644. [[CrossRef](#)]
- Magnozzi, M.; Pflug, T.; Ferrera, M.; Pace, S.; Ramón, L.; Olbrich, M.; Canepa, P.; Ağircan, H.; Horn, A.; Forti, S.; et al. Local Optical Properties in CVD-Grown Monolayer WS₂ Flakes. *J. Phys. Chem. C* **2021**, *125*, 16059–16065. [[CrossRef](#)]
- Zhu, Z.Y.; Cheng, Y.C.; Schwingenschlögl, U. Giant Spin-Orbit-Induced Spin Splitting in Two-Dimensional Transition-Metal Dichalcogenide Semiconductors. *Phys. Rev. B Cover. Condens. Matter Mater. Phys.* **2011**, *84*, 153402. [[CrossRef](#)]
- Li, J.; Han, J.; Li, H.; Fan, X.; Huang, K. Large-Area, Flexible Broadband Photodetector Based on WS₂ Nanosheets Films. *Mater. Sci. Semicond. Process* **2020**, *107*, 104804. [[CrossRef](#)]
- Tan, H.; Fan, Y.; Zhou, Y.; Chen, Q.; Xu, W.; Warner, J.H. Ultrathin 2D Photodetectors Utilizing Chemical Vapor Deposition Grown WS₂ with Graphene Electrodes. *ACS Nano* **2016**, *10*, 7866–7873. [[CrossRef](#)] [[PubMed](#)]

24. Xue, Y.; Zhang, Y.; Liu, Y.; Liu, H.; Song, J.; Sophia, J.; Liu, J.; Xu, Z.; Xu, Q.; Wang, Z.; et al. Scalable Production of a Few-Layer MoS₂/WS₂ Vertical Heterojunction Array and Its Application for Photodetectors. *ACS Nano* **2016**, *10*, 573–580. [[CrossRef](#)]
25. Ye, K.; Liu, L.; Liu, Y.; Nie, A.; Zhai, K.; Xiang, J.; Wang, B.; Wen, F.; Mu, C.; Zhao, Z.; et al. Lateral Bilayer MoS₂–WS₂ Heterostructure Photodetectors with High Responsivity and Detectivity. *Adv. Opt. Mater.* **2019**, *7*, 1900815. [[CrossRef](#)]
26. Susarla, S.; Kutana, A.; Hachtel, J.A.; Kochat, V.; Apte, A.; Vajtai, R.; Idrobo, J.C.; Yakobson, B.I.; Tiwary, C.S.; Ajayan, P.M. Quaternary 2D Transition Metal Dichalcogenides (TMDs) with Tunable Bandgap. *Adv. Mater.* **2017**, *29*, 1702457. [[CrossRef](#)]
27. Mann, J.; Ma, Q.; Odenthal, P.M.; Isarraraz, M.; Le, D.; Preciado, E.; Barroso, D.; Yamaguchi, K.; von Son Palacio, G.; Nguyen, A.; et al. 2-Dimensional Transition Metal Dichalcogenides with Tunable Direct Band Gaps: MoS_{2(1-x)}Se_{2x} Monolayers. *Adv. Mater.* **2014**, *26*, 1399–1404. [[CrossRef](#)]
28. Wang, Z.; Liu, P.; Ito, Y.; Ning, S.; Tan, Y.; Fujita, T.; Hirata, A.; Chen, M. Chemical Vapor Deposition of Monolayer Mo_{1-x}W_xS₂ Crystals with Tunable Band Gaps. *Sci. Rep.* **2016**, *6*, 21536. [[CrossRef](#)]
29. Mouloua, D.; Kotbi, A.; Deokar, G.; Kaja, K.; el Marssi, M.; el Khakani, M.A.; Jouiad, M. Recent Progress in the Synthesis of MoS₂ Thin Films for Sensing, Photovoltaic and Plasmonic Applications: A Review. *Materials* **2021**, *14*, 3283. [[CrossRef](#)]
30. Liu, H.F.; Wong, S.L.; Chi, D.Z. CVD Growth of MoS₂-Based Two-Dimensional Materials. *Chem. Vap. Depos.* **2015**, *21*, 241–259. [[CrossRef](#)]
31. Zhao, W.; Ghorannevis, Z.; Amara, K.K.; Pang, J.R.; Toh, M.; Zhang, X.; Kloc, C.; Tan, P.H.; Eda, G. Lattice Dynamics in Mono- and Few-Layer Sheets of WS₂ and WSe₂. *Nanoscale* **2013**, *5*, 9677–9683. [[CrossRef](#)]
32. Lan, F.; Lai, Z.; Xu, Y.; Cheng, H.; Wang, Z.; Qi, C.; Chen, J.; Zhang, S. Synthesis of Vertically Standing MoS₂ Triangles on SiC. *Sci. Rep.* **2016**, *6*, 31980. [[CrossRef](#)] [[PubMed](#)]
33. Rajput, N.S.; Kotbi, A.; Kaja, K.; Jouiad, M. Long-Term Aging of CVD Grown 2D-MoS₂ Nanosheets in Ambient Environment. *npj Mater. Degrad.* **2022**, *6*, 75. [[CrossRef](#)]
34. Zhao, W.; Pan, J.; Fang, Y.; Che, X.; Wang, D.; Bu, K.; Huang, F. Metastable MoS₂: Crystal Structure, Electronic Band Structure, Synthetic Approach and Intriguing Physical Properties. *Chemistry—Eur. J.* **2018**, *24*, 15942–15954. [[CrossRef](#)]
35. Wang, L.; Kutana, A.; Yakobson, B.I. Many-Body and Spin-Orbit Effects on Direct-Indirect Band Gap Transition of Strained Monolayer MoS₂ and WS₂. *Ann. Phys.* **2014**, *526*, L7–L12. [[CrossRef](#)]
36. Brumme, T.; Calandra, M.; Mauri, F. First-Principles Theory of Field-Effect Doping in Transition-Metal Dichalcogenides: Structural Properties, Electronic Structure, Hall Coefficient, and Electrical Conductivity. *Phys. Rev. B Cover. Condens. Matter Mater. Phys.* **2015**, *91*, 155436. [[CrossRef](#)]
37. Li, W.; Wang, T.; Dai, X.; Wang, X.; Zhai, C.; Ma, Y.; Chang, S.; Tang, Y. Electric Field Modulation of the Band Structure in MoS₂/WS₂ van Der Waals Heterostructure. *Solid State Commun.* **2017**, *250*, 9–13. [[CrossRef](#)]
38. dos Santos, R.B.; Rivelino, R.; Mota, F.D.B.; Kakanakova-Georgieva, A.; Gueorguiev, G.K. Feasibility of Novel (H₃C)_NX(SiH₃)_{3-n} Compounds (X = B, Al, Ga, In): Structure, Stability, Reactivity, and Raman Characterization from Ab Initio Calculations. *Dalton Trans.* **2015**, *44*, 3356–3366. [[CrossRef](#)]
39. Kakanakova-Georgieva, A.; Giannazzo, F.; Nicotra, G.; Cora, I.; Gueorguiev, G.K.; Persson, P.O.Å.; Pécz, B. Material Proposal for 2D Indium Oxide. *Appl. Surf. Sci.* **2021**, *548*, 149275. [[CrossRef](#)]
40. Mukherjee, B.; Tseng, F.; Gunlycke, D.; Amara, K.K.; Eda, G.; Simsek, E. Complex Electrical Permittivity of the Monolayer Molybdenum Disulfide (MoS₂) in near UV and Visible. *Opt. Mater. Express* **2015**, *5*, 447. [[CrossRef](#)]
41. Vaquero, D.; Clericò, V.; Salvador-Sánchez, J.; Martín-Ramos, A.; Díaz, E.; Domínguez-Adame, F.; Meziani, Y.M.; Diez, E.; Quereda, J. Excitons, Trions and Rydberg States in Monolayer MoS₂ Revealed by Low-Temperature Photocurrent Spectroscopy. *Commun. Phys.* **2020**, *3*, 194. [[CrossRef](#)]
42. Mouloua, D.; Rajput, N.S.; Blach, J.-F.; Lejeune, M.; El Marssi, M.; El Khakani, M.A.; Jouiad, M. Fabrication Control of MoS₂/MoO₂ Nanocomposite via Chemical Vapor Deposition for Optoelectronic Applications. *Mater. Sci. Eng. B* **2022**, *286*, 116035. [[CrossRef](#)]
43. Landi, S.; Segundo, I.R.; Freitas, E.; Vasilevskiy, M.; Carneiro, J.; Tavares, C.J. Use and Misuse of the Kubelka-Munk Function to Obtain the Band Gap Energy from Diffuse Reflectance Measurements. *Solid State Commun.* **2022**, *341*, 114573. [[CrossRef](#)]
44. Tan, H.; Xu, W.; Sheng, Y.; Lau, C.S.; Fan, Y.; Chen, Q.; Tweedie, M.; Wang, X.; Zhou, Y.; Warner, J.H. Lateral Graphene-Contacted Vertically Stacked WS₂/MoS₂ Hybrid Photodetectors with Large Gain. *Adv. Mater.* **2017**, *29*, 1702917. [[CrossRef](#)] [[PubMed](#)]
45. Kufer, D.; Konstantatos, G. Highly Sensitive, Encapsulated MoS₂ Photodetector with Gate Controllable Gain and Speed. *Nano Lett.* **2015**, *15*, 7307–7313. [[CrossRef](#)]
46. Taffelli, A.; Dirè, S.; Quaranta, A.; Pancheri, L. MoS₂ Based Photodetectors: A Review. *Sensors* **2021**, *21*, 2758. [[CrossRef](#)] [[PubMed](#)]
47. Liu, X.; Hu, S.; Lin, Z.; Li, X.; Song, L.; Yu, W.; Wang, Q.; He, W. High-Performance MoS₂ Photodetectors Prepared Using a Patterned Gallium Nitride Substrate. *ACS Appl. Mater. Interfaces* **2021**, *13*, 15820–15826. [[CrossRef](#)] [[PubMed](#)]
48. Han, P.; Marie, L.S.; Wang, Q.X.; Quirk, N.; El Fatimy, A.; Ishigami, M.; Barbara, P. Highly Sensitive MoS₂ Photodetectors with Graphene Contacts. *Nanotechnology* **2018**, *29*, 20LT01. [[CrossRef](#)]
49. Kim, B.H.; Gu, H.H.; Yoon, Y.J. Large-Area and Low-Temperature Synthesis of Few-Layered WS₂ Films for Photodetectors. *2D Mater.* **2018**, *5*, 045030. [[CrossRef](#)]

50. Zeng, L.; Tao, L.; Tang, C.; Zhou, B.; Long, H.; Chai, Y.; Lau, S.P.; Tsang, Y.H. High-Responsivity UV-Vis Photodetector Based on Transferable WS₂ Film Deposited by Magnetron Sputtering. *Sci. Rep.* **2016**, *6*, 20343. [[CrossRef](#)]
51. Lan, C.; Zhou, Z.; Zhou, Z.; Li, C.; Shu, L.; Shen, L.; Li, D.; Dong, R.; Yip, S.P.; Ho, J.C. Wafer-Scale Synthesis of Monolayer WS₂ for High-Performance Flexible Photodetectors by Enhanced Chemical Vapor Deposition. *Nano Res.* **2018**, *11*, 3371–3384. [[CrossRef](#)]

Disclaimer/Publisher's Note: The statements, opinions and data contained in all publications are solely those of the individual author(s) and contributor(s) and not of MDPI and/or the editor(s). MDPI and/or the editor(s) disclaim responsibility for any injury to people or property resulting from any ideas, methods, instructions or products referred to in the content.